Multispectral Imaging-Based System for Detecting Tissue Oxygen Saturation With Wound Segmentation for Monitoring Wound Healing

CHIH-LUNG LIN [1], **(Senior Member, IEEE), MENG-HSUAN WU** [1]**, YUAN-HAO HO** [1]**,**
FANG-YI LIN [1]**, (Student Member, IEEE), YU-HSIEN LU** [1]**,**
YUAN-YU HSUEH [2,3]**, AND CHIA-CHEN CHEN** [1]

[1]Department of Electrical Engineering, National Cheng Kung University, Tainan 70101, Taiwan
[2]Division of Plastic and Reconstructive Surgery, National Cheng Kung University Hospital, Tainan 70428, Taiwan
[3]Department of Surgery, National Cheng Kung University Hospital, Tainan 70428, Taiwan
CORRESPONDING AUTHOR: C.-L. LIN (cllin@ee.ncku.edu.tw)

ABSTRACT Objective: Blood circulation is an important indicator of wound healing. In this study, a tissue oxygen saturation detecting (TOSD) system that is based on multispectral imaging (MSI) is proposed to quantify the degree of tissue oxygen saturation (StO_2) in cutaneous tissues. Methods: A wound segmentation algorithm is used to segment automatically wound and skin areas, eliminating the need for manual labeling and applying adaptive tissue optics. Animal experiments were conducted on six mice in which they were observed seven times, once every two days. The TOSD system illuminated cutaneous tissues with two wavelengths of light - red ($\lambda = 660$ nm) and near-infrared ($\lambda = 880$ nm), and StO_2 levels were calculated using images that were captured using a monochrome camera. The wound segmentation algorithm using ResNet34-based U-Net was integrated with computer vision techniques to improve its performance. Results: Animal experiments revealed that the wound segmentation algorithm achieved a Dice score of 93.49%. The StO_2 levels that were determined using the TOSD system varied significantly among the phases of wound healing. Changes in StO_2 levels were detected before laser speckle contrast imaging (LSCI) detected changes in blood flux. Moreover, statistical features that were extracted from the TOSD system and LSCI were utilized in principal component analysis (PCA) to visualize different wound healing phases. The average silhouette coefficients of the TOSD system with segmentation (ResNet34-based U-Net) and LSCI were 0.2890 and 0.0194, respectively. Conclusion: By detecting the StO_2 levels of cutaneous tissues using the TOSD system with segmentation, the phases of wound healing were accurately distinguished. This method can support medical personnel in conducting precise wound assessments.

INDEX TERMS Multispectral imaging, principal component analysis, tissue oxygen saturation, wound healing, wound segmentation.

Clinical and Translational Impact Statement—This study supports efforts in monitoring StO_2 levels, wound segmentation, and wound healing phase classification to improve the efficiency and accuracy of preclinical research in the field.

I. INTRODUCTION

WOUND care is a medical problem that affects quality of life. During a period of wound healing, wound infections can lead to cellulitis, septicemia, and even lower limb amputation, increasing the burden of care on patients' families and generating extra medical expenses [1], [2].

Wounds have traditionally been assessed by visual inspection by trained medical personnel, which is subjective and non-quantitative [3]. Therefore, wound assessment tools that provide quantitative information are important in ensuring the effectiveness of medical treatments and preventing the deterioration of wounds.

To determine the status of a wound healing, the characteristics of the wounds, such as blood flow and oxygenation, can be utilized to assess the blood circulation of cutaneous tissues [4]. Transcutaneous oximetry (TcPO$_2$) [5], [6], [7] was developed to determine the oxygen concentration of the skin. TcPO$_2$ is a contact method that uses electrodes to heat a small region of skin and measure the partial pressure of oxygen (PaO$_2$) in the cutaneous tissue. The level of PaO$_2$ can help to determine the quality of blood circulation near a wound, helping medical personnel in conducting comprehensive wound assessments. Nevertheless, TcPO$_2$ can only be applied to healthy skin to evaluate wound healing indirectly, and measuring a stable oxygen pressure requires half of an hour. Therefore, along with the rapid development of wearable technology [8], [9], [10], [11], [12], smart bandages with flexible circuits and embedded oxygen sensors have been developed to monitor directly the oxygen concentration of wounds [13], [14], [15]. However, the use of smart bandages with contact dressings on wounds can lead to patient discomfort and infections, and so is unfavorable in clinical practice.

Recently, various optical technologies that permit noncontact measurement in a short time have been widely used in wound imaging [16], [17], [18]. Laser doppler imaging (LDI) [19], [20], [21] and laser speckle contrast imaging (LSCI) [22], [23], [24] are two real-time methods for measuring hemodynamic changes. In LDI and LSCI, the movement of red blood cells within cutaneous tissues is illuminated by a laser. Then, changes in the frequency and speckling of the reflected laser light are captured to estimate blood perfusion and flux, respectively. However, the clinical application of LDI and LSCI is limited by the expense of the procedures and their susceptibility to interference by ambient light. Consequently, hyperspectral imaging (HSI) has been developed as a technique that can provide reliable results even in environments that are affected by ambient light [25], [26], [27]. In HSI, a broadband light source and a hyperspectral camera are used to capture images at a series of wavelengths. Based on the difference in the optical properties of cutaneous tissues, the captured images are utilized to acquire oxygenation parameters, such as oxyhemoglobin (HbO$_2$), deoxyhemoglobin (Hb), and tissue oxygen saturation (StO$_2$). However, HSI requires complex calculation processes and high computational power to deal with a large number of captured images that are required. Therefore, multispectral imaging (MSI) has been developed; it uses simple hardware structures to capture a few specific spectra, yielding the same parameters as HSI [28], [29], [30]. MSI has a lower cost, uses simpler hardware structures, and requires less computational power than LDI, LSCI, and HSI. All of methods in the studies that are cited above require the manual labeling of wound and skin areas, which is time-consuming and subjective, yielding results that vary among practitioners [31], [32]. Furthermore, since the reflectance of incident light differs between the wound and skin tissues when the epidermis is wounded, the StO$_2$ levels need to be calculated separately [35], [36], [37]. Thus, wound and skin tissues must be labeled to enhance the accuracy of wound assessment using the MSI system. These labels can also be utilized in applying the corresponding reflectance of incident light in the calculation of the StO$_2$ levels.

In this study, an MSI-based tissue oxygen saturation detecting (TOSD) system with a wound segmentation algorithm is proposed to measure the StO$_2$ levels of cutaneous tissues in vivo. The wound segmentation algorithm can be used to annotate wound and skin tissues, which are used to determine the size of the wound area and calculate the StO$_2$ levels by applying the corresponding reflectance of light. To evaluate the performance of the TOSD system on cutaneous tissues, animal experiments were conducted on six wild-type mice of which seven observations were made every two days. The Dice score of the wound segmentation algorithm is 93.49%. A comparison of statistical results, including analysis of variance (ANOVA) and principal component analysis (PCA), with those concerning blood flux that are obtained using a commercially available LSCI (Moor FLPI-2, Moor Instruments, UK) reveals that the TOSD system is more effective than LSCI in identifying phases of wound healing.

II. MATERIALS AND METHODS
A. ANIMAL PREPARATION AND PROCEDURE
All animal experiments were approved by the Institutional Animal Care and Use Committee at the National Cheng Kung University, Taiwan (Approval No. 110089). Eight-week-old (n = 6) C57BL/6 male mice that weighed approximately 20 g each were used. All mice were housed in an environment-controlled room (temperature: 18-25 °C, humidity: 55% $\pm$ 5%, light: 12-hour light/dark cycle, light cycle starting at 07:00) at the National Laboratory Animal Center (Tainan, Taiwan) with sufficient food and water. To observe the changes in StO$_2$ levels throughout the wound healing period, a full-thickness wound was made on the dorsum of each mouse by experienced doctors. During surgery, mice were anesthetized with isoflurane that was mixed with 0.2 L/min oxygen and 0.8 L/min air through a face mask. To make wounds of the same size in all mice, a biopsy punch was utilized to punch a 6 mm diameter circular hole in the dorsum of each mouse after the mouse fur had been removed. To avoid wound contraction, a 1 mm thick silicone splint was applied with internal and external diameters of 8 and 12 mm, respectively. The splint was placed around the perimeter of each wound and secured with six interrupted 5-0 nylon sutures. In the animal experiments, wounds were
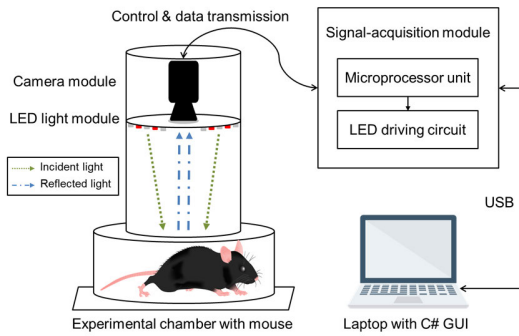
FIGURE 1. Hardware architecture of proposed TOSD system. USB: universal serial bus; GUI: graphical user interface.
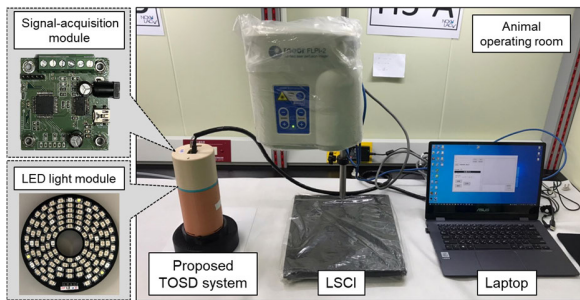

FIGURE 2. System setup of the animal experiments.

observed using the TOSD system every two days from Day 0 (the day of surgery) to Day 12.

To identify transitions among wound healing phases, the Enzyme-Linked Immunosorbent Assay (ELISA) kit was utilized as the clinical ground truth. Secretions and mucus from a wound site were collected on Day 2, Day 6, and Day 12 and homogenized with RIPA Lysis and Extraction Buffer (Cat. #89900 and 89901, Thermo Fisher Scientific®, Waltham, MA, USA), containing a protease inhibitor cocktail (Catalog No. C0001, TargetMol). The protein concentration was determined using a PierceTM BCA Protein Assay Kit (Cat. #23225, Thermo Fisher Scientific®, Waltham, MA, USA) and subjected to analysis on a RayBio® C-Series Mouse Angiogenesis Antibody Array C1, using the manufacturer's reagents and protocols. The density of each spot was visualized using a Touch Imager (e-BLOT; Shanghai, China) and determined using ImageJ software (Version 1.53e).

B. IMAGING SYSTEMS AND EXPERIMENTAL SETUP

Fig. 1 shows the hardware architecture of the proposed TOSD system for StO₂ level detection and wound segmentation, including a light-emitting diode (LED) light module, a signal-acquisition module, a camera, an experimental chamber, and a laptop. The LED light module consists of LEDs of three types (660 nm for red light, 880 nm for near-infrared light, and white light) and so has different light sources for illuminating cutaneous tissues. The red and near-infrared light can penetrate the superficial skin to produce reflected and
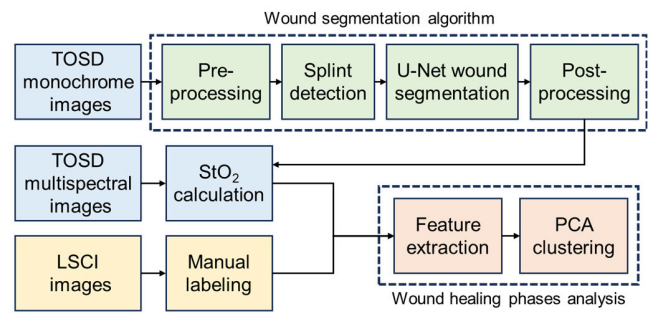

FIGURE 3. Block diagram of image data processing.

scattered light, which can be utilized to calculate the StO₂ levels [17]. White light is used to obtain images for wound segmentation. The signal-acquisition module is designed to drive the LED light module and switch among the light sources. The camera module consists of a monochrome camera (MB152USB, OMRON SENTECH, Japan) and an optical lens (M0814-MP2, COMPUTAR, USA), and is utilized to image wound and skin tissues. The images that are captured by the camera module are stored on the laptop using the universal serial bus (USB) protocol. The 3D printed experimental chamber is designed to fix the imaging distance between the monochrome camera and the mice for consistency in the animal experiments. For the convenience of users who are controlling the TOSD system, a graphical user interface is developed using the C# programming language.

To compare imaging results of the proposed TOSD system, the LSCI equipment (moorFLPI-2, Moor Instruments, UK.) was utilized. The resolution of this camera is 2064 × 1544, and the distance between the camera and the measured object is 25 cm, fixed using two aiming lasers. The light source that illuminates the measured object comprises infrared laser diodes with a center wavelength of 785 nm. Fig. 2 presents the system setup of the animal experiments, including the proposed TOSD system, LSCI, and a laptop for recording experimental data. These imaging data from the animal experiments are processed and analyzed to obtain wound segmentation results and wound healing phases of mice, as shown in Fig. 3.

C. WOUND SEGMENTATION ALGORITHM AND TRAINING SETUP

To determine the StO₂ levels in cutaneous tissues, a wound segmentation algorithm is proposed to segment wound and skin areas, as shown in Fig. 3. The algorithm has the following four stages: 1) pre-processing (pre-pr.), 2) splint detection (SD), 3) wound segmentation (WS), and 4) post-processing (post-pr.). The pre-pr. technique is often used in data processing to improve the quality of signals and images [38], [39], [40]. Thus, in the pre-pr. stage, the original image (with pixel dimensions of 800 × 800) is processed by histogram equalization to expand the grayscale range of the

Algorithm 1 The hole-filling technique.

Input:	The segmentation result of prediction is denoted as $n \times n$ matrix S, $S[i,j] \in \{$ wound label; background label $\}$, where $1 \leq i, j \leq n$
	A set of borders $BS = \{B_1, B_2, \ldots, B_N \mid \text{Area}(B_{k-1}) < \text{Area}(B_k), 1 < k \leq N\}$, where B_k is the outer border of the wound mask, N is the number of wound masks, and Area (B_k) denotes the number of $S[i,j]$ inside B_k
Output:	The segmentation result after hole-filling is denoted as $n \times n$ matrix S', $S'[i,j] \in \{$ wound label; background label $\}$, where $1 \leq i, j \leq n$

```
 1:  S' ← S
 2:  for all B_k of BS do
 3:     if (Area(B_k) < 10) then
 4:        for all S[i, j] in B_k do
 5:           S'[i, j] ← background label
 6:        end for
 7:     else
 8:        for all S[i, j] in B_k do
 9:           S'[i, j] ← wound label
10:        end for
11:     end if
12:  end for
13:  return S'
```

original image, improving the performance of the wound segmentation algorithm [41]. Next, in the SD stage, the Hough Transform technique is utilized to find the silicone splint, which is in the shape of an annulus, and the original image is cropped to 160×160 pixels based on the detected annulus [42]. Then, in the WS stage, the cropped image is imported into a U-Net for wound segmentation. To improve the accuracy and reduce the training time of U-Net, the technique of transfer learning (TL) is implemented [43]. Finally, in the post-pr. stage, the noise of the segmentation masks was eliminated using the hole-filling technique in Algorithm 1. The segmentation masks include labels of three types: 1) wound labels, 2) skin labels, and 3) background labels. The skin labels are determined based on the SD process; specifically, the pixels inside the area of the silicone splint, which are not segmented as wound labels, are regarded as skin labels. For U-Net training, the Adam optimizer is used to optimize the weights of U-Net. The training hyperparameters of learning rate and the mini-batch size of U-Net are set to 0.0001 and 4, respectively. The number of training epochs is 200. The ground truth of segmentation masks were provided by an experienced plastic surgeon at National Cheng Kung University Hospital, Tainan, Taiwan.

Five animal experiments were conducted in this study; each involved collecting images of wound in mice utilizing the proposed tissue oxygen saturation detecting (TOSD) system with illumination by white light. However, only the 5th experiment was conducted with both TOSD and LSCI. Therefore, the results of the first four experiments were only used in wound segmentation and not in the wound healing phase classification. The data were randomly assigned to either a training set or a testing set, with 90% of the images used for training (208 images) and 10% used for testing (23 images).

D. EVALUATION METRICS

Four indices [44], [45] were used to evaluate segmentation performance, they are precision, recall, the Dice similarity coefficient, and intersection-over-union (IoU), calculated as follows:

$$Precision = TP/(TP + FP) \qquad (1)$$

$$Recall = TP/(TP + FN) \qquad (2)$$

$$Dice = 2TP/(2TP + FP + FN) \qquad (3)$$

$$IoU = TP/(TP + FP + FN) \qquad (4)$$

where TP, TN, FP, and FN are true positive, true negative, false positive and false negative pixel numbers of wound images, respectively.

E. FUNDAMENTAL THEORY OF CUTANEOUS TISSUE OPTICS

To obtain the StO₂ levels from images that are captured by the TOSD system, the optics in cutaneous tissues must be considered. When light is applied to cutaneous tissues, the surface reflects some of it, and the remaining light is absorbed and scattered by chromophores, which are the main elements in cutaneous tissues that affect light propagation. Thus, two wavelengths of light (660 nm and 880 nm) at which the optical properties of oxyhemoglobin (HbO₂) and deoxyhemoglobin (Hb) maximally differ are used to calculate the StO₂ levels [46]. To determine the propagation of light in cutaneous tissues, the modified Beer-Lambert law (MBLL) [47], which describes the relationship between light and chromophores, is used:

$$\text{OD}_\lambda = \ln(I_i - I_r)/(I_s - I_r) = \varepsilon C d_\lambda \qquad (5)$$

where λ is the wavelength of the light source; OD_λ is the optical density, which is the sum of the absorbances in cutaneous tissues; I_i is the intensity of incident light; I_r is the intensity of reflected light, and I_s is the intensity of the diffuse light. ε and C are the absorption coefficient and the concentration of chromophores, respectively. d_λ is the maximum depth of penetration of the light in cutaneous tissues [48].

The optical properties of mouse skin in the visible and near-infrared spectrum [49], and the relationship between the optical reflectances of wound and skin tissues [33] are such that the intensity of the reflected light I_r can be expressed as follows:

$$I_r = R_\lambda I_i, \quad R_\lambda = \begin{cases} R_\lambda^W, & \text{for wound tissues} \\ R_\lambda^S, & \text{for skin tissues} \end{cases} \qquad (6)$$

where R_λ is the reflectance of cutaneous tissues, which depends on the results that are generated by the wound segmentation algorithm, and R_λ^W and R_λ^S represent the reflectances of wound and skin tissues, respectively. In this study, the R_{660}^W and R_{660}^S of red light ($\lambda = 660$ nm) are set to 0.15 and 0.2, respectively, and the R_{880}^W and R_{880}^S of near-infrared light ($\lambda = 880$ nm) are set to 0.11 and 0.15, respectively. Therefore, by calculating the intensity of light captured by the TOSD system, the value of OD_{660} and OD_{880} are obtained; these are used to compute the concentration

of chromophores in (5). The cutaneous tissues contain the following four chromophores: 1) water, 2) other, 3) HbO$_2$, and 4) Hb. Based on the additivity of light absorbance, the OD$_\lambda$ of cutaneous tissues can be obtained by summing the OD$_\lambda$ values of all chromophores [50], as follows:

$$OD_\lambda = (\varepsilon_{water}C_{water} + \varepsilon_{other}C_{other} + \varepsilon_{HbO_2}C_{HbO_2} + \varepsilon_{Hb}C_{Hb})d_\lambda \tag{7}$$

In (7), C_{Hb} and C_{HbO_2} are the only two unknown values, and the other values are constants or calculated. Therefore, two wavelengths suffice to obtain C_{Hb} and C_{HbO_2}, and calculate the StO$_2$ levels of cutaneous tissues as follows:

$$c_{Hb} = \frac{\varepsilon_{HbO_2}^{\lambda_2}(OD^{\lambda_1}/d^{\lambda_1}) - \varepsilon_{HbO_2}^{\lambda_1}(OD^{\lambda_2}/d^{\lambda_2})}{\varepsilon_{Hb}^{\lambda_1}\varepsilon_{HbO_2}^{\lambda_2} - \varepsilon_{Hb}^{\lambda_2}\varepsilon_{HbO_2}^{\lambda_1}} \tag{8}$$

$$c_{HbO_2} = \frac{\varepsilon_{Hb}^{\lambda_1}(OD^{\lambda_2}/d^{\lambda_2}) - \varepsilon_{Hb}^{\lambda_2}(OD^{\lambda_1}/d^{\lambda_1})}{\varepsilon_{Hb}^{\lambda_1}\varepsilon_{HbO_2}^{\lambda_2} - \varepsilon_{Hb}^{\lambda_2}\varepsilon_{HbO_2}^{\lambda_1}} \tag{9}$$

$$StO_2 = C_{HbO_2}/(C_{Hb} + C_{HbO_2}) \times 100\% \tag{10}$$

where StO$_2$ represents the level of tissue oxygenation in wound and skin tissues.

F. WOUND HEALING PHASES ANALYSIS

To classify the phases of wound healing in mice, statistical features of wound and skin tissues, including wound size, average (AVG) of blood flux and StO$_2$, and standard deviation (STD) of blood flux and StO$_2$, were extracted from the imaging results obtained using LSCI and the TOSD system, as given in Table 1. In the animal experiments, all observations were categorized into four wound healing phases based on the number of days after wounding and the results of the ELISA kit, as follows. 1) Day 0 for hemostasis, 2) Day 2 for inflammation, 3) Day 4-10 for proliferation, and 4) Day 12 for remodeling [51]. Principal component analysis (PCA) is utilized as the clustering method to visualize the distribution of data concerning wound healing phases [52]. Five features identified using both the TOSD system and LSCI are mapped into a two-dimensional space for PCA. The silhouette coefficient SC is adapted for each data point to quantify the clustering performance of PCA [53]; it is defined as follows:

$$SC(i) = (b(i) - a(i))/\max(a(i), b(i)) \tag{11}$$

$$a(i) = \frac{1}{N_x - 1} \sum_{j \in N_x, i \neq j} d(i, j) \tag{12}$$

where $a(i)$ represents the cohesiveness of data points and is the average distance between i and other points in the same cluster. Let N_x be the number of points cluster x and $d(i, j)$ be the distance between points i and j in N. The calculation of $b(i)$ is similar to that of $a(i)$ and yields the average distance from point i to all points in another most adjacent cluster.

$$b(i) = \min_{j \neq 1} \frac{1}{N_x} \sum_{j \in N_x} d(i, j) \tag{13}$$

TABLE 1. Statistical features extracted from LSCI and proposed TOSD system.

System	Feature
LSCI	Wound_size
	Blood_flux_wound_average
	Blood_flux_wound_standard_deviation
	Blood_flux_skin_average
	Blood_flux_skin_standard_deviation
Proposed TOSD system	Wound_size
	StO$_2$_wound_average
	StO$_2$_wound_standard_deviation
	StO$_2$_skin_average
	StO$_2$_skin_standard_deviation

The SC value ranges from -1 to 1. An SC value closing to 1 represents an excellent clustering performance. An SC value closing to -1 represents an unreliable clustering performance.

III. RESULTS

A. WOUND SEGMENTATION ALGORITHM

Fig. 4 displays the segmentation results that were obtained using different wound segmentation algorithms. To validate the robustness of wound segmentation using the algorithm, images with varying sizes of wounds are used. The sizes of the wounds are determined by calculating the dimensions of the fixed silicone splints with consistent diameters. The segmentation masks that are generated by the algorithm can be utilized to evaluate visually the performance of each method. The method that uses only U-Net may incompletely segment wounds, as demonstrated in sample 4 of Fig. 4. Therefore, the SD process is applied to refine the training images. The SD+U-Net method can generate rough wound masks with some inaccurate outlines, which may not be sufficiently precise to separate wound and skin areas. Thus, the technique of TL is implemented to improve the performance of U-Net. Although the masks of the SD+U-Net+TL method were highly consistent with the ground truths, the noise can be clearly observed in the segmentation masks (black dotted circles in Fig. 4), including holes and small pixels outside the mask outline. Hence, the post-pr. process is utilized, and its results reveal that the noise of segmentation masks was completely removed. Therefore, the SD+U-Net+TL+post-pr. method can provide accurate segmentation masks of wound and skin areas for the calculation of StO$_2$ levels.

Table 2 lists the values of the evaluation metrics for different methods and the method in a previous work [32]. The mean Dice and IoU scores of the SD+U-Net method were 85.52% and 75.67%, respectively, higher than those, 70.84% and 59.06%, of the U-Net method. Applying the TL technique increased the mean Precision and IoU score of the SD+U-Net+TL method by 7.94% and 12.16%, respectively. Ultimately, the proposed method (SD+U-Net+TL+post-pr.) outperformed other methods (with Precision: 94.47%, Recall:
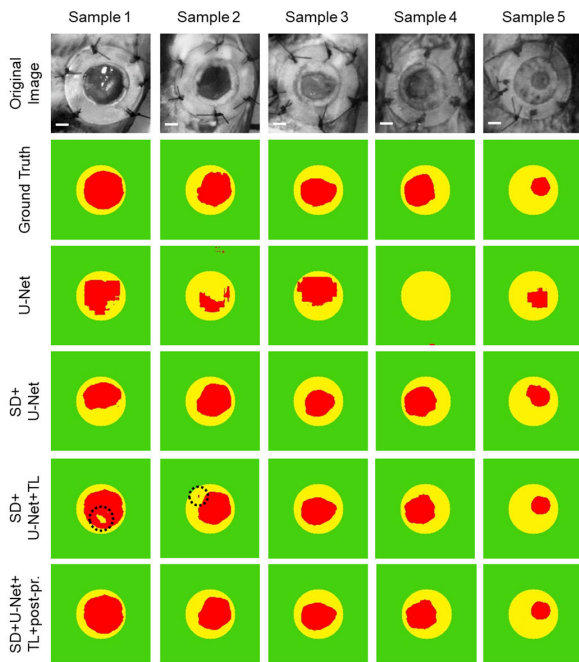
FIGURE 4. Wound segmentation results obtained using different methods. Wound, skin, and background labels are shown in red, yellow, and green, respectively. All scale bars represent 2 mm.

TABLE 2. Performance of wound segmentation algorithms.

Methods	Precision (%)	Recall (%)	Dice (%)	IoU (%)
Previous work [32]	N/A	N/A	86.65	81.64
U-Net	89.18 ± 22.40	61.69 ± 25.49	70.84 ± 23.9	59.06 ± 24.19
SD+U-Net	89.92 ± 9.79	84.03 ± 15.16	85.52 ± 8.85	75.67 ± 12.93
SD+U-Net+TL	94.44 ± 4.77	92.88 ± 5.12	93.46 ± 2.62	87.83 ± 4.61
SD+U-Net+TL+post-pr.	**94.47 ± 4.75**	**92.90 ± 5.09**	**93.49 ± 2.60**	**87.88 ± 4.56**

TABLE 3. Performance of different segmentation models.

Models	Size	Precision (%)	Recall (%)	Dice (%)	IoU (%)
MobileNetV2 [33]	3.5M	83.04 ± 16.66	77.70 ± 16.35	77.86 ± 11.64	65.07 ± 14.64
EfficientNetB3 [34]	12.3M	**95.05 ± 4.63**	91.24 ± 6.90	92.83 ± 3.29	86.79 ± 5.67
Proposed model (ResNet34-based)	21.3M	94.47 ± 4.75	**92.90 ± 5.09**	**93.49 ± 2.60**	**87.88 ± 4.56**

92.90%, Dice score: 93.49%, and IoU score: 87.88%). Additionally, the mean Dice and IoU scores of the proposed method were 6.84% and 6.24%, better than those achieved in the previous work, respectively [32]. Moreover, in the context of using particular pre-processing and post-processing methods, Table 3 displays the performance of the proposed U-Net model (ResNet34-based) and other segmentation models. The mean Dice and IoU scores of the proposed model were 93.49% and 87.88%, respectively, higher than those, 77.86% and 65.07%, of the MobileNetV2. Despite the proposed model's being the largest, its mean Dice and IoU scores were 0.66% and 1.09% better, respectively, than those of the second largest model (EfficientNetB3). These results of the animal experiments demonstrated that the proposed model (ResNet34-based) can accurately segment wound and skin areas.

B. StO$_2$ AND BLOOD FLUX EVALUATION IN ANIMAL EXPERIMENTS

Fig. 5 presents the imaging results of the animal experiments. A full-thickness wound was created on the dorsal skin of each mouse to observe the StO$_2$ levels throughout the wound healing period. LSCI was utilized to measure blood flux for comparison with the StO$_2$ levels that were obtained from the TOSD system. Monochrome images and heatmaps of blood flux and StO$_2$ were recorded every two days from Day 0 to Day 12, showing only the area inside silicone splints. Fig. 5(a) displays the monochrome images that were acquired from the TOSD system. The outward appearance of wounds during the wound healing period is provided.

Fig. 5(b) provides blood flux heatmaps that were captured by LSCI. The center of the wound can be clearly observed in a high blood flux. However, water and other materials in wounds can invalidate blood flux imaging by LSCI (gray pixels in Fig. 5(b)). Fig. 5(c) displays StO$_2$ heatmaps that were obtained from the TOSD system. In the wound area, StO$_2$ levels initially increased and then decreased. Specifically, the StO$_2$ levels in the wound area on Day 4 were higher than those on Day 2. Subsequently, the StO$_2$ levels remained high, before declining to the baseline level (Day 0) on Day 12. The skin area near the wound exhibited a similar trend (black dotted areas in Fig. 5 (c)). The red dotted areas in Fig. 5 have low StO$_2$ levels and invalid blood flux results, both of which are caused by the mouse fur. This phenomenon can be observed on other days, but does not affect the wound assessment.

Table 4 compare StO$_2$ levels and blood flux in wound and skin tissues on different days, respectively. The collected data on blood flux and StO$_2$ levels from six mice were analyzed using one-way ANOVA, with a significance level of 0.05. The StO$_2$ levels in wound tissues increased significantly from Day 0 (85.11 ± 1.12%) to Day 2 (88.59 ± 1.22%) and remained at an average of over 88% from Day 2 to Day 10. On Day 12, the StO$_2$ levels in wound tissues (86.84 ± 0.68%) dropped significantly to close to the baseline level (Day 0). The StO$_2$ levels in skin tissues exhibited a similar trend to those in wound tissues. However, the blood flux in wound tissues did not significantly differ between Day 0 (339.47 ± 110.48 PU) and Day 2 (313.30 ± 54.05 PU) but it had increased significantly by Day 4 (587.03 ± 149.75 PU). The blood flux in the wound tissues remained elevated from Day 4 to Day 12, averaging above 500 PU. The blood flux in the skin tissues exhibited a similar trend to that observed in the wound tissues. These results demonstrate that the TOSD system detected changes in both wound and skin tissues earlier than did LSCI.
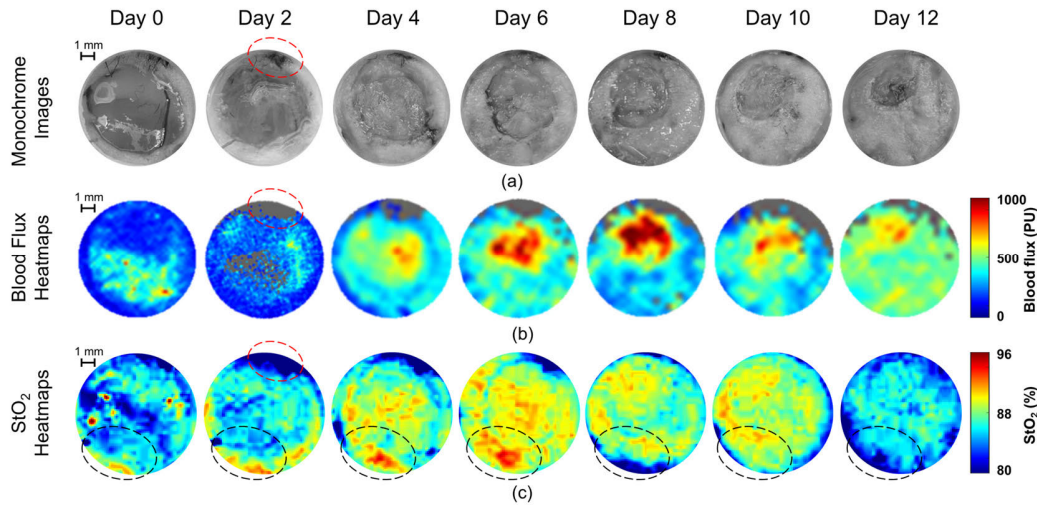
FIGURE 5. Imaging results of animal experiments (a) monochrome images, (b) blood flux heatmaps, and (c) StO₂ heatmaps.

TABLE 4. Mean and standard deviation of StO₂ level and blood flux in animal experiments.

System	Tissue type	Day 0	Day 2	Day 4	Day 6	Day 8	Day 10	Day 12
TOSD	Wound (%) (Mean ± Std. Dev.)	85.11 ± 1.12	88.59 ± 1.22	88.35 ± 0.67	88.64 ± 1.18	88.60 ± 0.51	88.35 ± 2.64	86.84 ± 0.68
	p-value	N/A	0.0035	0.0081	0.0029	0.0033	0.0007	n.s.
	Skin (%) (Mean ± Std. Dev.)	84.72 ± 1.12	88.40 ± 1.76	86.69 ± 1.66	86.68 ± 1.44	86.92 ± 1.23	87.58 ± 1.87	85.58 ± 1.25
	p-value	N/A	0.003	n.s.	n.s.	n.s.	0.0269	n.s.
LSCI	Wound (PU) (Mean ± Std. Dev.)	339.47 ± 110.48	313.30 ± 54.05	587.03 ± 149.75	654.40 ± 107.14	710.40 ±88.08	541.80 ± 129.86	610.77 ± 126.79
	p-value	N/A	n.s.	0.0104	0.0097	0.0019	n.s.	0.0340
	Skin (PU) (Mean ± Std. Dev.)	264.80± 102.14	207.46± 55.02	471.00 ± 112.41	527.21 ± 112.39	543.86 ± 130.72	419.63 ± 129.75	501.15 ± 100.65
	p-value	N/A	n.s.	0.0006	0.0074	0.0102	n.s.	0.0265

n.s. means no significant differences. All p-values are calculated based on the data on Day 0.
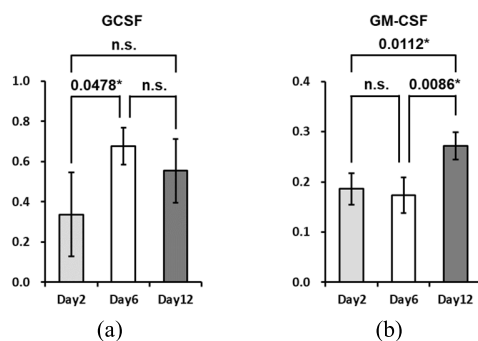

FIGURE 6. Analyzed results of ELISA kit (a) GCSF (b) GM-CSF. n.s. means no significant differences.

C. WOUND HEALING PHASES ANALYSIS

To identify transitions among wound healing phases, an angiogenesis ELISA kit was utilized following the manufacturer's instructions. Two key factors that have significant changes during the wound healing process were selected [54]. In Fig. 6 (a), the level of signature cytokine of the proliferation phase, the Granulocyte-Colony Stimulating Factor (GCSF), increased significantly from Day 2 to Day 6 (with the p-value = 0.0478), indicating a transition from the inflammatory phase (Day 2) to the proliferation phase (Day 6) in the wound healing process. In Fig. 6 (b), the Granulocyte–macrophage colony-stimulating factor (GM-CSF), which is capable of regulating inflammatory response and promoting collagen proliferation, had increased significantly on Day 12 (with p-values = 0.0112 and 0.0086 compared to Day 2 and Day 6, respectively) [54]. These results indicate that the wound on Day 12 might have been entering the remodeling phase. Therefore, the wound healing phases of mice were identified as the hemostasis phase (Day 0) the inflammatory phase (Day 2), the proliferation phase (Day 4 to Day 10), and the tissue remodeling phase (Day 12).

Fig. 7 presents the clustering results of PCA that are obtained using LSCI and the TOSD system. Table 5 quantifies the clustering performance of PCA associated with
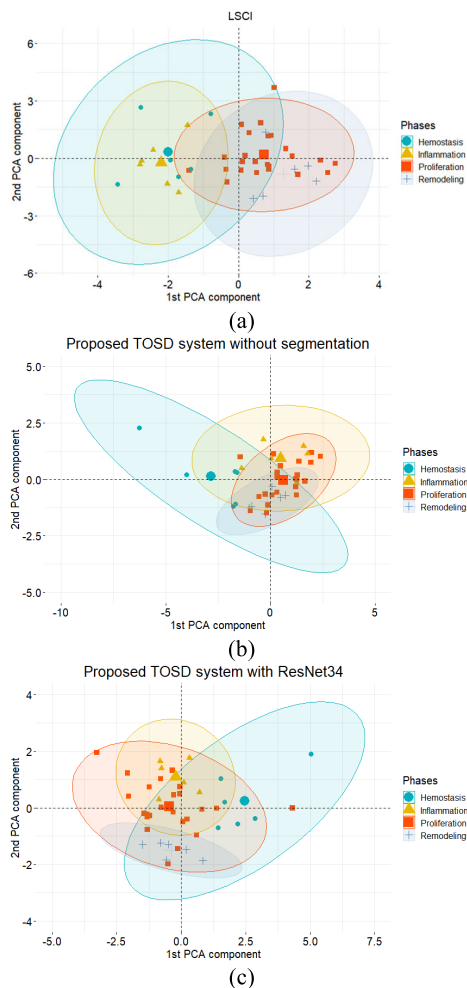
FIGURE 7. PCA scatter plots of all observations of animal experiments in different wound healing phases (a) LSCI, (b) proposed TOSD system without segmentation, (c) proposed TOSD system with ResNet34 (proposed U-Net model).

TABLE 5. Silhouette coefficients of wound healing phases of LSCI and proposed TOSD system.

Wound Healing phase	Silhouette coefficient				
	LSCI	Proposed TOSD system			
		Without segmentation	With MobileNetV2	With EfficientNetB3	With ResNet34
Hemostasis	-0.4218	-0.1543	0.0509	0.2244	**0.2791**
Inflammation	0.2903	-0.0331	0.2584	0.3220	**0.6114**
Proliferation	**0.0160**	-0.1475	-0.5367	-0.4890	-0.4849
Remodeling	0.1932	0.5083	-0.1930	0.7261	**0.7504**
Average	0.0194	0.0434	-0.1051	0.1959	**0.2890**

healing phases, and the performance of wound segmentation can significantly impact the classification of wound healing phases.

IV. DISCUSSION

Several approaches evaluating wound healing have been used in clinical practice, and these compared with the proposed TOSD system in Table 6. Smart bandages are a contact method that carries the risk of infection. Optoacoustic imaging (OAI) is an imaging modality that combines the advantages of optical and acoustic imaging techniques [55]. It is particularly well-suited for imaging vascular structures. Therefore, OAI is a promising and effective imaging method in the future. However, current OAI often uses high-power lasers that carry the risk of eye and skin injury. Moreover, the complex hardware architecture and excessive cost of OAI are two of the bottlenecks in its clinical translation applications [56]. Noncontact optical techniques for providing valuable information about wound characteristics, such as blood flux and StO₂ levels during the wound healing period, have been rapidly developed; they include LDI, LSCI, HIS, and MSI, [16], [17], [18]. Among these, MSI offers a short measurement time (less than 3 seconds) and a sufficient imaging depth (3 mm). Therefore, MSI stands out as a relatively simple hardware structure and cost-effective method with the potential to accurately measure StO₂ levels for the assessment of wounds in clinical practice [28], [29], [30]. Importantly, however, wound and skin areas must be labeled after performing MSI to obtain the distribution of StO₂ levels within a wound. While most relevant studies have focused on measuring wound characteristics, the labeling of wounds is crucial for in-depth wound analysis [31], [32]. Hence, a wound characteristic imaging must be combined with segmentation to enhance the efficiency and accuracy of wound diagnosis. In this study, the TOSD system based on MSI is integrated with a wound segmentation algorithm to investigate in vivo the changes in StO₂ levels during the healing period of wounds in mice. The algorithm provides objective segmentation masks of wounds for calculating StO₂ levels, which are used to evaluate blood circulation in wound and skin tissues. Changes in blood flux that are obtained by LSCI are compared to the results of the TOSD system, and the transitions of wound healing phases with and without segmentation are discussed.

each wound healing phase and the average value of four wound healing phases. Figs. 7 (a), (b), and (c) display PCA scatter plots of all observations that were made in the animal experiments using LSCI, the TOSD system without segmentation, and the TOSD system with ResNet34 (proposed U-Net model), respectively. Each wound healing phase is presented with the average value of all data points and an elliptical area of 95% confidence, enabling visualization of the distribution of data among wound healing phases. In Fig. 7, the TOSD system yielded a stronger clustering result than LSCI. The clustering results of the TOSD system with ResNet34 show an improvement in separating different phases compared to the results without segmentation. Moreover, as given in Table 5, the silhouette coefficients of the TOSD system with ResNet34 generally exceeded those of other methods, except in the proliferation phase. The average silhouette coefficient of the TOSD system with ResNet34 was 0.2890, greater than that of EfficientNetB3. These results indicate that the proposed TOSD system outperforms LSCI in classifying wound

TABLE 6. Comparison of proposed TOSD system and other works.

	Mostafalu [13]	Naidi [55]	Couturier [24]	Schmidt [27]	Park [30]	Proposed TOSD system
Sensing technique	Oxygen sensor	OAI	LSCI	HSI	MSI	MSI
Physiological parameters	Oxygen concentration	Blood flux Oxygen saturation	Blood flux	Oxygen saturation	Oxygen saturation	Oxygen saturation
Noncontact	No	Yes	Yes	Yes	Yes	Yes
Imaging depth of wounds	N/A	depends on the system setup	1 mm	3-6 mm	3 mm	3 mm
Measurement time	Continuous	Continuous	3 sec	6 sec	Continuous	3 sec
Wound segmentation	No	No	No	No	No	Yes
Adaptive tissue optics	No	No	No	No	No	Yes
Healing phase classification	No	No	No	No	No	Yes

From the results in Fig. 4 and Table 2, the U-Net method yielded overly fragmented segmentation masks of wounds compared to the ground truths; perhaps due to the oversizing of training images (with dimensions of 800 × 800 pixels), which contain large areas of unnecessary pixels that may reduce the performance of the feature extraction layers in U-Net. Thus, the process of SD is applied in a manner similar to its application in a previous work in which YOLOv3 was used to detect wounds and crop original wound images for U-Net training. Therefore, the SD+U-Net method yields much better Dice and IoU scores than the U-Net method, yielding similar values of the evaluation metrics to those reported elsewhere [32]. However, some inaccuracies are presented in the edges of the wound masks and the ground truths, perhaps owing to the use of insufficient training images, which might have caused underfitting by U-Net. Notably, the scarcity of training data is a common challenge in deep learning networks for biomedical applications [58]. Therefore, the technique of TL that can converge the weights of U-Net faster and better is utilized. The results showed that the segmentation masks generated by the SD+U-Net+TL method have more precise outlines compared to the SD+U-Net method. In most segmentation tasks, there is a possibility of encountering issues related to noise, which refers to irrelevant or erroneous information in the segmentation results that needs to be eliminated [31]. For example, holes and small pixels that appear outside wound outlines (black dotted circles in Fig. 4) could affect wound assessment. Moreover, the performances of lightweight models and the proposed model were compared in Table 3. In this study, the primary consideration is the accuracy of wound segmentation models. Lightweight models, such as MobileNetV2, lose performance due to the lightweight and efficient design of the network architecture to increase inference speed and reduce computational burden [31], [33]. Therefore, the U-Net model that is based on ResNet34 with a deeper and more complex architecture than that of MobileNetV2 was utilized in the proposed TOSD system. However, in the near future, the portable version of the proposed TOSD system might be implemented with lightweight models to reduce computational power and reduce inference time.

The observed wound healing phases in the animal experiments are identified as the hemostasis phase (Day 0) the inflammatory phase (Day 2), the proliferation phase (Day 4 to Day 10), and the tissue remodeling phase (Day 12) [51]. On day 0, following the formation of a wound, inflammatory cells migrate to the wounded area to prevent infection and secrete angiogenic factors [57]. Subsequently, new blood vessels begin to sprout from the wound edge towards the center of the wound, and the StO$_2$ levels increase [59]. Thus, StO$_2$ levels in both wound and skin tissues on Day 2 were significantly higher than those on Day 0 (with p-values = 0.0035 and 0.0030, respectively). However, the blood flux that was measured by LSCI in wound and skin tissues on Day 2 was not significantly higher than that of Day 0 (with both p-values > 0.05), perhaps because of the difference in penetration depths between MSI and LSCI. The TOSD system has the potential to penetrate to a depth of 3 mm, based on the wavelengths that were used in this study [60]. In contrast, the penetration depth of LSI is less than 1 mm [61], [62], [63]. On Day 2, new blood vessels had not yet grown to the surface of the wound, so LSCI was unable to observe changes in deeper wound tissues, resulting in similar blood flux measurements as on Day 0. Thus, following the growth of blood vessels, the blood flux in wound and skin tissues on Day 4 was significantly higher than that on Day 0 (with p-values = 0.0104 and 0.0006, respectively). Next, during the proliferation phase, new blood vessels proliferated continuously to form a mature vascular network, which provided wound tissues with sufficient oxygen supplements to heal. Therefore, the high values of StO$_2$ levels and blood flux in wound tissues from Day 4 to Day 10 indicated

that the wound area had a favorable healing status (with all p-values < 0.05, except for the blood flux on Day 10). Finally, during the tissue remodeling phase, microvessels started to regress and the oxygenation level gradually returned to the baseline level (Day 0). Thus, StO$_2$ levels in wound and skin tissues on Day 12 had dramatically dropped and were not significantly different from those on Day 0 (with both p-values > 0.05). However, the blood flux in wound and skin tissues differed significantly (with p-values $= 0.0340$ and 0.0265, respectively), indicating that the blood flow remained elevated. The high StO$_2$ at skin tissues adjacent to the wound tissues in Fig. 5 during the healing process are also consistent with those in other studies [64], [65], [66]. The StO$_2$ levels on different days indicated that the TOSD system can be used to identify wound healing phases. Moreover, the changes in wound and skin tissues can be visualized to assess wound healing progress.

Fig. 7 compares the clustering results of PCA in wound healing phases for LSCI and the TOSD system. In the PCA scatter plot for the TOSD system with ResNet34 (proposed U-Net model), minor overlaps between phases of wound healing are observed as expected, as they are consistent with the transitional nature of wound healing [67]. However, in the PCA scatter plot of LSCI, major overlaps are evident between the hemostasis phase and the inflammation phase, as well as between the proliferation phase and the remodeling phase. Moreover, the PCA clustering results with ResNet34 exhibited greater separability, compared to those without segmentation. Notably, in Fig. 7 (b), the inflammation, proliferation, and remodeling phases are strongly overlapped, indicating that the method without segmentation cannot identify the wound healing phases accurately. These clustering performances of PCA are quantified, with the TOSD system using ResNet34 showing average silhouette coefficients of 0.2696 and 0.2456 greater than those of LSCI and without segmentation, respectively. Therefore, the proposed TOSD system with ResNet34 demonstrates superior performance in classifying wound healing phases using statistical features of wound and skin tissues compared to LSCI and without segmentation.

LSCI has been commonly used for imaging blood flux in cutaneous tissues to evaluate blood circulation. However, LSCI can only target the surface of wounds due to its limited penetration depth. Therefore, MSI-based systems with deeper penetration are more suitable than LSCI for assessing wound healing status. Currently, the TOSD system provides only StO$_2$ levels in wound and skin tissues. However, future research, particularly that concerning human chronic wounds, must expand the analysis to consider the presence of different types of wound tissue, including granulation, slough, and necrosis. These tissue types have different outward appearances and significant roles in the wound healing process [2]. Incorporating additional wavelengths of light into the TOSD system enables other important wound characteristics, such as water content and metabolism, to be captured and analyzed [4]. This expanded analysis has the potential to provide a comprehensive understanding of wound status, facilitating improved diagnosis and treatment strategies for chronic wounds.

V. CONCLUSION

In this study, an MSI-based TOSD system is proposed to determine the StO$_2$ levels of cutaneous tissues in vivo. The implemented wound segmentation algorithm effectively distinguishes between wound and skin areas, generating objective segmentation masks that can be used to calculate accurate StO$_2$ levels by applying adaptive tissue optics. The mean Dice and IoU scores of the proposed wound segmentation algorithm are 93.49% and 87.88%, respectively. A comparison of animal experimental results with blood flux measurements that are obtained using LSCI demonstrates that the TOSD system yields a stronger correlation between determined StO$_2$ levels and wound healing dynamics. The variations in StO$_2$ levels at different wound healing phases were significant. Moreover, the TOSD system can be utilized to observe changes in wound healing phases before LSCI can be used, and it exhibits a higher average silhouette coefficient (0.2890) than that of LSCI (0.0194). Therefore, the TOSD system with segmentation algorithm is a promising prototype method for assessing wound healing status and blood circulation in human tissues, supporting wound care.

REFERENCES

[1] Y. Lucas, R. Niri, S. Treuillet, H. Douzi, and B. Castaneda, "Wound size imaging: Ready for smart assessment and monitoring," *Adv. Wound Care*, vol. 10, no. 11, pp. 641–661, Nov. 2021.

[2] C. K. Sen, "Human wound and its burden: Updated 2020 compendium of estimates," *Adv. Wound Care*, vol. 10, no. 5, pp. 281–292, May 2021.

[3] S. Greatrex-White and H. Moxey, "Wound assessment tools and nurses' needs: An evaluation study," *Int. Wound J.*, vol. 12, no. 3, pp. 293–301, Jun. 2015.

[4] C. Thomas Hess, "Checklist for factors affecting wound healing," *Adv. Skin Wound Care*, vol. 24, no. 4, p. 192, Apr. 2011.

[5] M. B. Strauss, B. J. Bryant, and G. B. Hart, "Transcutaneous oxygen measurements under hyperbaric oxygen conditions as a predictor for healing of problem wounds," *Foot Ankle Int.*, vol. 23, no. 10, pp. 933–937, Oct. 2002.

[6] M. Löndahl, P. Katzman, C. Hammarlund, A. Nilsson, and M. Landin-Olsson, "Relationship between ulcer healing after hyperbaric oxygen therapy and transcutaneous oximetry, toe blood pressure and ankle–brachial index in patients with diabetes and chronic foot ulcers," *Diabetologia*, vol. 54, no. 1, pp. 65–68, Oct. 2010.

[7] W. L. Yip, "Evaluation of the clinimetrics of transcutaneous oxygen measurement and its application in wound care," *Int. Wound J.*, vol. 12, no. 6, pp. 625–629, Dec. 2015.

[8] S. M. R. Islam, D. Kwak, M. H. Kabir, M. Hossain, and K. Kwak, "The Internet of Things for health care: A comprehensive survey," *IEEE Access*, vol. 3, pp. 678–708, 2015.

[9] C.-L. Lin, H.-C. Wu, T.-Y. Liu, M.-H. Lee, T.-S. Luo, and S.-T. Young, "A portable monitor for fetal heart rate and uterine contraction," *IEEE Eng. Med. Biol. Mag.*, vol. 16, no. 6, pp. 80–84, Nov. 1997.

[10] C.-L. Lin et al., "Innovative head-mounted system based on inertial sensors and magnetometer for detecting falling movements," *Sensors*, vol. 20, no. 20, p. 5774, Oct. 2020.

[11] C.-L. Lin, W.-C. Chiu, F.-H. Chen, Y.-H. Ho, T.-C. Chu, and P.-H. Hsieh, "Fall monitoring for the elderly using wearable inertial measurement sensors on eyeglasses," *IEEE Sensors Lett.*, vol. 4, no. 6, pp. 1–4, Jun. 2020.

[12] C.-L. Lin, Y.-H. Ho, W.-C. Chiu, T.-C. Chu, and Y.-H. Liu, "Innovative shoe-integrated system based on time-of-flight range sensors for fall detection on various terrains," *IEEE Sensors Lett.*, vol. 5, no. 10, pp. 1–4, Oct. 2021.

[13] P. Mostafalu, W. Lenk, M. R. Dokmeci, B. Ziaie, A. Khademhosseini, and S. R. Sonkusale, "Wireless flexible smart bandage for continuous monitoring of wound oxygenation," *IEEE Trans. Biomed. Circuits Syst.*, vol. 9, no. 5, pp. 670–677, Oct. 2015.

[14] G. Wang et al., "Stretchable optical sensing patch system integrated heart rate, pulse oxygen saturation, and sweat pH detection," *IEEE Trans. Biomed. Eng.*, vol. 66, no. 4, pp. 1000–1005, Apr. 2019.

[15] S.-Y. Lu et al., "Wireless multimodality sensing system-on-a-chip with time-based resolution scaling technique and analog waveform generator in 0.18 μm CMOS for chronic wound care," *IEEE Trans. Biomed. Circuits Syst.*, vol. 15, no. 6, pp. 1268–1282, Dec. 2021.

[16] M. Jayachandran, S. Rodriguez, E. Solis, J. Lei, and A. Godavarty, "Critical review of noninvasive optical technologies for wound imaging," *Adv. Wound Care*, vol. 5, no. 8, pp. 349–359, Aug. 2016.

[17] D. W. Paul et al., "Noninvasive imaging technologies for cutaneous wound assessment: A review," *Wound Repair Regeneration*, vol. 23, no. 2, pp. 149–162, Mar. 2015.

[18] G. Saiko, P. Lombardi, Y. Au, D. Queen, D. Armstrong, and K. Harding, "Hyperspectral imaging in wound care: A systematic review," *Int. Wound J.*, vol. 17, no. 6, pp. 1840–1856, Dec. 2020.

[19] J. Y. Shin and H. S. Yi, "Diagnostic accuracy of laser Doppler imaging in burn depth assessment: Systematic review and meta-analysis," *Burns*, vol. 42, no. 7, pp. 1369–1376, Nov. 2016.

[20] S. N. Jan et al., "Comparison of laser Doppler imaging (LDI) and clinical assessment in differentiating between superficial and deep partial thickness burn wounds," *Burns*, vol. 44, no. 2, pp. 405–413, Mar. 2018.

[21] C. Wearn et al., "Prospective comparative evaluation study of laser Doppler imaging and thermal imaging in the assessment of burn depth," *Burns*, vol. 44, no. 1, pp. 124–133, Feb. 2018.

[22] K. Basak, G. Dey, M. Mahadevappa, M. Mandal, D. Sheet, and P. K. Dutta, "Learning of speckle statistics for in vivo and noninvasive characterization of cutaneous wound regions using laser speckle contrast imaging," *Microvascular Res.*, vol. 107, pp. 6–16, Sep. 2016.

[23] T. M. van Vuuren et al., "Prediction of venous wound healing with laser speckle imaging," *Phlebol., J. Venous Disease*, vol. 32, no. 10, pp. 658–664, Jul. 2017.

[24] A. Couturier, R. Bouvet, J.-L. Cracowski, and M. Roustit, "Reproducibility of high-resolution laser speckle contrast imaging to assess cutaneous microcirculation for wound healing monitoring in mice," *Microvascular Res.*, vol. 141, May 2022, Art. no. 104319.

[25] Q. Yang et al., "Investigation of the performance of hyperspectral imaging by principal component analysis in the prediction of healing of diabetic foot ulcers," *J. Imag.*, vol. 4, no. 12, p. 144, Dec. 2018.

[26] M.-C. Chang et al., "Multimodal sensor system for pressure ulcer wound assessment and care," *IEEE Trans. Ind. Informat.*, vol. 14, no. 3, pp. 1186–1196, Mar. 2018.

[27] A. Schmidt, F. Nießner, T. von Woedtke, and S. Bekeschus, "Hyperspectral imaging of wounds reveals augmented tissue oxygenation following cold physical plasma treatment in vivo," *IEEE Trans. Radiat. Plasma Med. Sci.*, vol. 5, no. 3, pp. 412–419, May 2021.

[28] S. P. Philimon, A. K. C. Huong, and X. T. I. Ngu, "An alternative wavelength range for noninvasive assessment of wound tissue oxygenation status," *Int. J. Eng. Technol.*, vol. 7, no. 26, pp. 73–77, Jan. 2018.

[29] J. J. Squiers et al., "Machine learning analysis of multispectral imaging and clinical risk factors to predict amputation wound healing," *J. Vascular Surgery*, vol. 75, no. 1, pp. 279–285, Jan. 2022.

[30] Y.-R. Park, Y.-K. Shin, and J. B. Eom, "Non-contact oxygen saturation monitoring for wound healing process using dual-wavelength simultaneous acquisition imaging system," *Biomed. Eng. Lett.*, vol. 13, no. 3, pp. 455–463, Apr. 2023.

[31] C. Wang et al., "Fully automatic wound segmentation with deep convolutional neural networks," *Sci. Rep.*, vol. 10, no. 1, pp. 1–9, Dec. 2020.

[32] H. Carrión, M. Jafari, M. D. Bagood, H. Yang, R. R. Isseroff, and M. Gomez, "Automatic wound detection and size estimation using deep learning algorithms," *PLoS Comput. Biol.*, vol. 18, no. 3, Mar. 2022, Art. no. e1009852.

[33] M. Sandler, A. Howard, M. Zhu, A. Zhmoginov, and L.-C. Chen, "MobileNetV2: Inverted residuals and linear bottlenecks," in *Proc. IEEE/CVF Conf. Comput. Vis. Pattern Recognit.*, Jun. 2018, pp. 4510–4520.

[34] A. Abedalla, M. Abdullah, M. Al-Ayyoub, and E. Benkhelifa, "Chest X-ray pneumothorax segmentation using U-Net with EfficientNet and ResNet architectures," *PeerJ Comput. Sci.*, vol. 7, p. e607, Jun. 2021.

[35] H. Kolárová and D. Ditrichová, "Contribution to the measurement of optical characteristics of the skin," *Acta Univ. Palackianae Olomucensis Fac. Med.*, vol. 125, pp. 215–224, Jan. 1990.

[36] E. S. Papazoglou, M. S. Weingarten, L. Zubkov, L. Zhu, S. Tyagi, and K. Pourrezaei, "Optical properties of wounds: Diabetic versus healthy tissue," *IEEE Trans. Biomed. Eng.*, vol. 53, no. 6, pp. 1047–1055, Jun. 2006.

[37] E. S. Papazoglou et al., "Changes in optical properties of tissue during acute wound healing in an animal model," *J. Biomed. Opt.*, vol. 13, no. 4, 2008, Art. no. 044005.

[38] S. Pereira, A. Pinto, V. Alves, and C. A. Silva, "Brain tumor segmentation using convolutional neural networks in MRI images," *IEEE Trans. Med. Imag.*, vol. 35, no. 5, pp. 1240–1251, May 2016.

[39] P. Liskowski and K. Krawiec, "Segmenting retinal blood vessels with deep neural networks," *IEEE Trans. Med. Imag.*, vol. 35, no. 11, pp. 2369–2380, Nov. 2016.

[40] C.-L. Lin et al., "Tracking touched trajectory on capacitive touch panels using an adjustable weighted prediction covariance matrix," *IEEE Trans. Ind. Electron.*, vol. 64, no. 6, pp. 4910–4916, Jun. 2017.

[41] H. Ibrahim and N. P. Kong, "Image sharpening using sub-regions histogram equalization," *IEEE Trans. Consum. Electron.*, vol. 55, no. 2, pp. 891–895, May 2009.

[42] H. Yuen, J. Princen, J. Illingworth, and J. Kittler, "Comparative study of Hough transform methods for circle finding," *Image Vis. Comput.*, vol. 8, no. 1, pp. 71–77, Feb. 1990.

[43] J. Deng, W. Dong, R. Socher, L.-J. Li, K. Li, and L. Fei-Fei, "ImageNet: A large-scale hierarchical image database," in *IEEE Conf. Comput. Vis. Pattern Recognit.*, Jun. 2009, pp. 248–255.

[44] K. Han et al., "An effective semi-supervised approach for liver CT image segmentation," *IEEE J. Biomed. Health Informat.*, vol. 26, no. 8, pp. 3999–4007, Aug. 2022.

[45] A. Haider, M. Arsalan, Y. W. Lee, and K. R. Park, "Deep features aggregation-based joint segmentation of cytoplasm and nuclei in white blood cells," *IEEE J. Biomed. Health Informat.*, vol. 26, no. 8, pp. 3685–3696, Aug. 2022.

[46] I. V. Meglinski and S. J. Matcher, "Quantitative assessment of skin layers absorption and skin reflectance spectra simulation in the visible and near-infrared spectral regions," *Physiol. Meas.*, vol. 23, no. 4, pp. 741–753, Oct. 2002.

[47] A. K. C. Huong, P. E. Ong, V. H. Tsen, and X. T. I. Ngu, "A handheld technology for optical monitoring of transcutaneous blood oxygen saturation," *Int. J. Eng. Technol.*, vol. 7, no. 3.20, p. 122, Sep. 2018.

[48] R. R. Anderson and J. A. Parrish, "The optics of human skin," *J. Investigative Dermatol.*, vol. 77, no. 1, pp. 13–19, Jul. 1981.

[49] C. P. Sabino et al., "The optical properties of mouse skin in the visible and near infrared spectral regions," *J. Photochemistry Photobiol. B, Biol.*, vol. 160, pp. 72–78, Jul. 2016.

[50] H.-Y. Tsai, K.-C. Huang, H.-C. Chang, J. A. Yeh, and C.-H. Chang, "A noncontact skin oxygen-saturation imaging system for measuring human tissue oxygen saturation," *IEEE Trans. Instrum. Meas.*, vol. 63, no. 11, pp. 2620–2631, Nov. 2014.

[51] A. Rege, N. V. Thakor, K. Rhie, and A. P. Pathak, "In vivo laser speckle imaging reveals microvascular remodeling and hemodynamic changes during wound healing angiogenesis," *Angiogenesis*, vol. 15, pp. 87–98, Dec. 2011.

[52] A. Shokouhmand et al., "Diagnosis of peripheral artery disease using backflow abnormalities in proximal recordings of accelerometer contact microphone (ACM)," *IEEE J. Biomed. Health Informat.*, vol. 27, no. 1, pp. 274–285, Jan. 2023.

[53] Z. Lin, F. Wen, Y. Ding, and Y. Xue, "Data-driven coherency identification for generators based on spectral clustering," *IEEE Trans. Ind. Informat.*, vol. 14, no. 3, pp. 1275–1285, Mar. 2018.

[54] S. Barrientos, H. Brem, O. Stojadinovic, and M. Tomic-Canic, "Clinical application of growth factors and cytokines in wound healing," *Wound Repair Regeneration*, vol. 22, no. 5, pp. 569–578, Sep. 2014.

[55] N. Sun et al., "Photoacoustic microscopy of vascular adaptation and tissue oxygen metabolism during cutaneous wound healing," *Biomed. Opt. Exp.*, vol. 13, no. 5, pp. 2695–2706, Apr. 2022.

[56] H. Assi et al., "A review of a strategic roadmapping exercise to advance clinical translation of photoacoustic imaging: From current barriers to future adoption," *Photoacoustics*, vol. 32, Aug. 2023, Art. no. 100539.

[57] S. Werner and R. Grose, "Regulation of wound healing by growth factors and cytokines," *Physiological Rev.*, vol. 83, no. 3, pp. 835–870, Jul. 2003.

[58] A. Yakimovich, A. Beaugnon, Y. Huang, and E. Ozkirimli, "Labels in a haystack: Approaches beyond supervised learning in biomedical applications," *Patterns*, vol. 2, no. 12, Dec. 2021, Art. no. 100383.

[59] S. Schreml, R. M. Szeimies, L. Prantl, S. Karrer, M. Landthaler, and P. Babilas, "Oxygen in acute and chronic wound healing," *Brit. J. Dermatology*, vol. 163, no. 2, pp. 257–268, Aug. 2010.

[60] F. Vasefi, N. MacKinnon, and D. L. Farkas, "Hyperspectral and multispectral imaging in dermatology," in *Imaging in Dermatology*. New York, NY, USA: Academic, Aug. 2016, pp. 187–201.

[61] J. Senarathna, A. Rege, N. Li, and N. V. Thakor, "Laser speckle contrast imaging: Theory, instrumentation and applications," *IEEE Rev. Biomed. Eng.*, vol. 6, pp. 99–110, 2013.

[62] M. A. Davis, S. M. S. Kazmi, and A. K. Dunn, "Imaging depth and multiple scattering in laser speckle contrast imaging," *J. Biomed. Opt.*, vol. 19, no. 8, Aug. 2014, Art. no. 086001.

[63] K. J. Zheng, E. Middelkoop, M. Stoop, P. P. M. van Zuijlen, and A. Pijpe, "Validity of laser speckle contrast imaging for the prediction of burn wound healing potential," *Burns*, vol. 48, no. 2, pp. 319–327, Mar. 2022.

[64] A. Huong and X. Ngu, "Optical visualization of skin oxygen saturation for dermatological applications," *Optik*, vol. 204, Feb. 2020, Art. no. 163948.

[65] W. Ren, Q. Gan, Q. Wu, S. Zhang, and R. Xu, "Quasi-simultaneous multimodal imaging of cutaneous tissue oxygenation and perfusion," *J. Biomed. Opt.*, vol. 20, no. 12, Sep. 2015, Art. no. 121307.

[66] Z. Yu et al., "Image-guided cold atmosphere plasma (CAP) therapy for cutaneous wound," *Proc. SPIE*, vol. 9698, pp. 64–76, Mar. 2016.

[67] N. X. Landén, D. Li, and M. Ståhle, "Transition from inflammation to proliferation: A critical step during wound healing," *Cellular Mol. Life Sci.*, vol. 73, no. 20, pp. 3861–3885, May 2016.

● ● ●